

# Geometric Feature Learning for 3D Meshes

Huan Lei, Naveed Akhtar, Mubarak Shah, and Ajmal Mian

**Abstract**—Geometric feature learning for 3D meshes is central to computer graphics and highly important for numerous vision applications. However, deep learning currently lags in hierarchical modeling of heterogeneous 3D meshes due to the lack of required operations and/or their efficient implementations. In this paper, we propose a series of modular operations for effective geometric deep learning over heterogeneous 3D meshes. These operations include mesh convolutions, (un)pooling and efficient mesh decimation. We provide open source implementation of these operations, collectively termed *Picasso*. The mesh decimation module of Picasso is GPU-accelerated, which can process a batch of meshes on-the-fly for deep learning. Our (un)pooling operations compute features for newly-created neurons across network layers of varying resolution. Our mesh convolutions include facet2vertex, vertex2facet, and facet2facet convolutions that exploit vMF mixture and Barycentric interpolation to incorporate fuzzy modelling. Leveraging the modular operations of Picasso, we contribute a novel hierarchical neural network, PicassoNet-II, to learn highly discriminative features from 3D meshes. PicassoNet-II accepts primitive geometrics and fine textures of mesh facets as input features, while processing full scene meshes. Our network achieves highly competitive performance for shape analysis and scene parsing on a variety of benchmarks. We release Picasso and PicassoNet-II on Github.

**Index Terms**—Geometric feature learning, Mesh convolution, 3D shape analysis, 3D scene parsing, GPU mesh decimation, Picasso.



## 1 INTRODUCTION

DISCRIMINATIVE feature extraction from 3D meshes is fundamentally important for computer graphics [1], [2] and computer vision [3], [4], [5]. Its success is of great value to multiple emerging technologies, including autonomous driving, robotics and virtual/augmented reality. Considering the impressive performance of convolutional feature learning on homogeneous grid data, i.e. images and videos [6], [7], [8], [9], [10], [11], [12], [13], researchers are also seeking alternative convolutional neural networks for 3D-mesh feature learning [1], [14], [15]. Currently this is a major research topic in geometric deep learning, which focuses on feature encoding of generic heterogeneous data in non-Euclidean space [16].

Compared to 3D point clouds, the geodesic connections of 3D meshes, that constitute edges and facets on top of vertices, hold key information about object surfaces and scene topology [3], [17]. Concurrently, mesh facets can also carry higher resolution texture information. This variety and heterogeneous nature of mesh data primitives (i.e. vertices, facets, textures, etc.), makes adaption of deep learning to 3D meshes much more challenging [18]. Besides, the rich extra information of mesh data casts large memory footprint on GPU devices, and raises practical concerns for the training of deep neural networks, especially in large-scale scenario [3], [4], [5], [19], [20].

Applications in computer graphics largely focus on small-scale mesh data. We find a few mesh-based neural networks to learn features for *shape analysis* [1], [2], [21], [22], [23]. Generally, these methods handle small shape meshes as graphs and learn mesh representations using graph convo-

lutions. Their architectures are either non-hierarchical that adopt a single network resolution, or they slowly reduce the network resolution with inefficient mesh decimation algorithms [24], [25], [26], [27]. Whereas non-hierarchical networks and slow resolution reduction are acceptable for small-scale problems, they become impractical for large-scale mesh data.

For large-scale 3D problems, e.g. *semantic scene parsing*, most techniques only deal with (voxelized) point clouds [18], [28], [29], [30], [31], [32], [33]. The absence of efficient modular operations for mesh processing in the modern libraries such as Tensorflow [34], Pytorch [35], requires substantial effort for deep learning application to large-scale mesh inputs. This is a currently major hindrance in effective neural modeling of scene surfaces [15], [36]. Point cloud methods are unable to directly benefit from the pre-existing neighborhood information in data. On the other hand, robust geometrics and fine facet texture of meshes provide appealing alternatives to point coordinates  $(x, y, z)$  and colors  $(r, g, b)$  as input features. These alternatives remain largely under-exploited in practical large-scale 3D problems due to the absence of appropriate operations in the contemporary deep learning libraries.

With this work, we aim to advance geometric deep learning over 3D meshes for shape analysis in graphics and scene parsing in vision. We introduce *Picasso*<sup>1</sup>, a collection of deep learning modules that provides convenient modular operations for efficient mesh decimation, (un-)pooling and convolution. Additionally, we propose a generic neural network for efficiently learning discriminative features for synthetic/real, small/large-scale, watertight/unstructured meshes. We construct our mesh-based neural network with the proposed Picasso modules. Our network processes facet geometrics and textures instead of vertex coordinates and colors as input, while also capitalizing on the pre-existing

• H. Lei, N. Akhtar and A. Mian are with the Department of Computer Science and Software Engineering, The University of Western Australia, 35 Stirling Highway, Crawley, Western Australia, 6009. M. Shah is with the Center for Research in Computer Vision, University of Central Florida, 4328 Scorpis St. Orlando, USA. E-mail: huan.lei@research.uwa.edu.au, naveed.akhtar@uwa.edu.au, shah@crco.ucf.edu, ajmal.mian@uwa.edu.au.

1. Paying homage to Pablo Picasso for cubism in paintings.

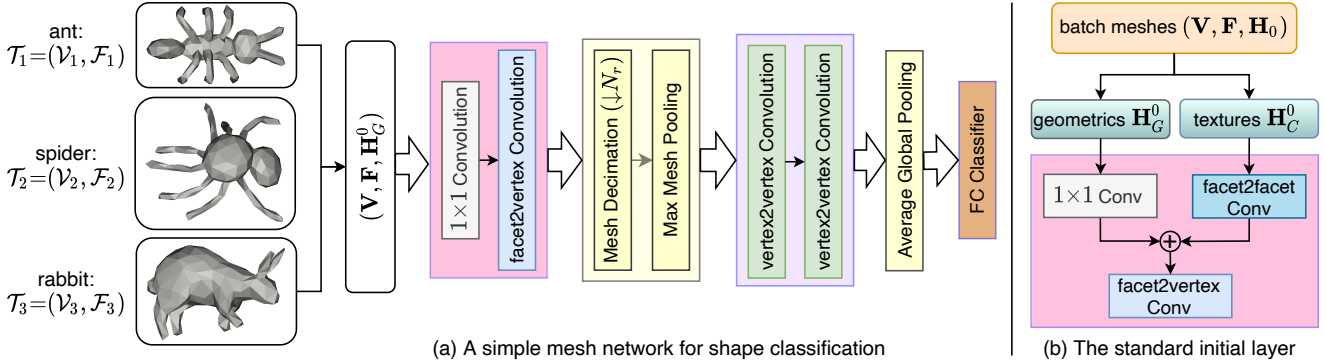


Fig. 1. (a) An example of building a simple hierarchical mesh network for shape classification using the mesh convolutions and poolings in Picasso. The network comprises two hierarchical layers, and uses batch size 3 in this example. It accepts batch input as a tuple of  $(\mathbf{V}, \mathbf{F}, \mathbf{H}_G^0)$ , where  $\mathbf{V}$  denotes concatenated vertices,  $\mathbf{F}$  are facets, and  $\mathbf{H}_G^0$  denotes facet geometric features of shapes. In this illustration, we decimate the input meshes by reducing their number of vertices by  $N_r$ . (b) Example configuration of the standard initial layer which considers the input features to comprise both geometric features,  $\mathbf{H}_G^0$ , and texture features,  $\mathbf{H}_C^0$ . We discuss further details of this figure in the overview of Picasso in § 5.

geodesic neighborhood of meshes.

In Picasso, we introduce GPU-accelerated mesh decimation that simplifies a *batch* of heterogeneous meshes on-the-fly for hierarchical feature learning. It performs all computations in parallel on GPU, except for the vertex clustering. It allows control over the decimated mesh resolution using a desired number of vertex. We define the (un)pooling operations based on vertex clusters recorded during the decimation. They are required to produce features for newly-created neurons when the network resolution is altered. In addition, three novel convolution types are presented for context aggregation on meshes, namely *facet2vertex*, *vertex2facet*, and *facet2facet*. The mesh convolutions exploit von Mises-Fisher (vMF) mixture [37] and Barycentric interpolation for different fuzzy modelling. Figure 1 illustrates an example mesh-based neural network for shape classification that can be built using Picasso modules.

We additionally propose a generic neural network for 3D meshes, PicassoNet-II, by incorporating a series of significant improvements in the original PicassoNet [38]. These improvements pertain to skip connections, dual convolutions, network depth and the ability to process true mesh data. Dual convolutions, that explore both geodesic and Euclidean neighborhoods, can be computationally intractable for dense data due to the search required to establish the Euclidean neighborhood [18]. We demonstrate that Euclidean neighborhood does not contribute significantly in feature learning from high-resolution meshes. Leveraging this insight PicassoNet-II applies dual convolutions only at the low-resolution layers. Our network is also able to process both small-scale and large-scale 3D meshes as intact samples alike. We evaluate PicassoNet-II on the ShapeNetCore [39] dataset, along with SHREC [40], CUBE [1], COSEG [41], Human [42] and FAUST [43] for shape analysis. We also evaluate it on the large-scale S3DIS [20] and ScanNet [3] datasets for real-world scene parsing, achieving highly competitive results in all cases.

This article is a significant extension of our preliminary work presented in IEEE CVPR 2021 [38]. Below, we summarize the major enhancements beyond the preliminary conference work.

- **Fuzzy modeling:** Since normals represent directional distributions on the surface of a unit sphere, we replace

the Gaussian mixture in [38] with the vMF mixture for better fuzzy modelling. Additionally, we train the centers (mean directions) of each mixture component while fixing its concentration parameter. We also remove the Barycentric interpolation of vertex2facet convolution in [38] for computational and memory gain.

- **Improved efficiency without trading-off efficacy:** We establish the passive role of dual convolutions in high-resolution mesh feature learning. In PicassoNet-II, we address this to gain significant computational advantage over [38] while maintaining the performance. We further improve the network architecture through better design choices for skip connections and sub-network blocks.
- **Rendered mesh as input:** The network in [38] can only process point coordinates and colors as input features, whereas PicassoNet-II can also handle rendered meshes as inputs. We incorporate all required functionalities in our network, including reconfiguration of the initial convolutional layer - see Fig. 1.
- **Extensive evaluation:** We evaluate PicassoNet-II for shape analysis and scene parsing on a wide variety of standard benchmarks. It achieves highly competitive performance on all datasets. We also provide extensive ablation studies for analysis. We release the latest Picasso and PicassoNet-II at Github<sup>2</sup> for the broader research community.
- **Pytorch extension:** Originally in [38], Picasso was implemented in Tensorflow. However, with this work, we make it available in both Tensorflow and Pytorch due to the growing popularity of Pytorch. We emphasize that Picasso version released with this article incorporates not only the newly introduced modules for heterogeneous mesh processing, but also compatible modular operations for heterogeneous point cloud processing. We include the point cloud modules by improving on our previous contributions to heterogeneous applications [18], [44]. As a whole, Picasso enables conveniently building of neural networks to process 3D meshes and point clouds of arbitrary sizes.

2. <https://github.com/EnyaHermite/Picasso>

## 2 RELATED WORK

Among the existing feature learning approaches for 3D data, the majority considers ‘point cloud’ as input, while only a few works deal with meshes despite their added benefits of pre-existing neighborhood connections. This discrepancy can be largely attributed to the absence of modular implementations that provide operations for hierarchical deep learning with fast mesh decimation and network reduction as well as (un)poolings.

### 2.1 Convolution on 3D Point Clouds

Applying voxel-grid kernels to dense volumetric representations is the most straightforward solution of transferring CNNs from images to point clouds [45], [46], [47], [48], [49], [50]. However, the practical potential of these methods is limited by their cubically growing requirements on memory and computational resources. Different strategies have been introduced to incorporate sparsity into the dense volumetric CNNs [28], [51], [52], [53], [54], [55], among which SparseConvNets [28], [52], [56] are currently the best performing architectures. Several approaches also explore similar regular-grid kernels for transformed input representations of point clouds, such as TangentConv [57], SplatNet [33], PCNN [58]. Since PointNet [59], the permutation invariant networks learn features from point clouds using multilayer perceptrons followed by max pooling [31], [32], [59], [60], [61], [62], [63] and show that the spatial coordinates  $(x, y, z)$  of points can be effective input features to the network.

Graph-based neural networks allow the convolutions to be conducted in either spectral or spatial domain. However, applying the spectral convolutions to point cloud processing is complicated because they demand the graph Laplacians of different input samples to be pre-aligned [64]. As a pioneering work in the spatial domain, ECC [65] exploits dynamical filters [66] to parameterize the graph convolutional parameters for point cloud analysis. Subsequent works also explored more effective kernel and filter parameterizations [31], [67], [68], [69], [70]. The discrete kernels [18], [29], [44], [71], [72] are efficient alternatives to those dynamic kernels as they define the filter parameters directly, avoiding the necessity of indirect filter generation within the network. The spherical kernels [18], [44] that separate depth-wise and point-wise computations are memory and runtime advantageous, while KPConv [29] is reported to be more competitive than SparseConvNets. Recently, researchers have also started to adapt transformers [73] to point cloud processing [74].

Although many existing approaches use spatial coordinates  $(x, y, z)$  of points as geometric input features (e.g. [29], [31], [32], [44], [44], [68], [69], [70]), they particularly lack convenience when data cropping and transformations are involved in pre-processing or data augmentation. Our work allows mesh structures as the input modality instead. The alternate of relative geometric attributes of mesh facets as the input feature naturally mitigates the problem.

### 2.2 Convolution on 3D Meshes

Multiple approaches exist that employ convolution on meshes to learn features for small-scale shape analysis. The convolutions are generally performed on local planar

patches defined in the hand-crafted coordinate systems [21], [22], [75]. These methods either establish the coordinate system using geodesic level sets [75] or surface normals and principle curvatures [21], [22]. For improved correspondence matching, Verma *et al.* [14] replaced the previous hand-crafted local patches with a learnable mapping between graph neighborhoods and filter weights. To reconstruct human facial expressions, Ranjan *et al.* [2] exploited the spectral graph convolutions [76] with hierarchical mesh-based autoencoders.

Whereas other methods focus on learning vertex-wise features, MeshCNN [1] introduces convolutional operation that learns edge-wise features for semantic labelling on a mesh. The recent PD-MeshNet [77] further extracts facet-wise representations by defining convolution on the primal-dual graphs of an input mesh. It reduces network resolution using the graph edge contraction method provided by Pytorch Geometric [78].

Currently, only a small number of mesh-based convolutional networks exist for large-scale scene parsing in the real world. TextureNet [36] parameterizes the room surface into local planar patches in the 4-RoS field such that standard CNNs [7] can be applied to extract high-resolution texture information from mesh facets. Schult *et al.* [15] applied the spatial graph convolutions of dynamic filters [31], [65], [68], [79] to the union of neighborhoods in both geodesic and Euclidean domains for vertex-wise feature learning. VMNet [80] combines the SparseConvNet [56] with graph convolutional networks to learn merged features from point clouds and meshes. Generally, previous methods explore mesh as an edge-based graph and define the graph convolutions based on its geodesic connections [2], [14], [15], [77]. We instead propose convolutions on the mesh structure itself, following its elementary geometric components, i.e. vertices and facets. To promote this more natural perspective, we also contribute computation and memory optimized CUDA implementations for forward and backward propagations of all the mesh convolutions we present in this work.

### 2.3 Mesh Decimation

Hierarchical neural networks induce multi-scale feature extraction by allowing convolutions to be applied on increasing receptive fields of the input data. Although farthest point sampling (FPS) is widely used to construct hierarchical architectures for point clouds [18], [31], [32], it is inapplicable to mesh processing because of its inability of tracking vertex connections. Fortunately, the graphics research community has contributed effective methods for mesh simplification, such as Vertex Clustering (VC) [26] and Quadric Error Metrics (QEM) [24], [25]. The two methods are suitable choices for mesh-based neural networks [2], [15], [80] to establish hierarchical architectures. Compared to VC, the QEM method is good at reducing mesh resolution while retaining most of its geometric information, leading to superior performance [15]. In specific, QEM simplifies a mesh via iterative contractions of vertex pairs, whereas the optimal vertex pair for contraction has to be determined after each iteration. The popular geometric processing library - Open3D [27], offers simplification functions for both VC and QEM. However, the CPU-based implementation is

inefficient and also not amenable to operations required for deep learning, e.g. batch processing.

Though superior to VC in performance, the iterative progressive strategy of QEM makes it impossible to be deployed on GPUs as parallel processes. In this work, we introduce a fast mesh decimation technique based on the QEM algorithm [25]. Compatible to deep learning, our method can process a batch of heterogeneous meshes on-the-fly. In contrast to [25], it sorts all the vertex pairs only once according to their quadric errors, and groups the vertices to be contracted into *disjoint* clusters. Except for the grouping process, all other computations in our method get accelerated via parallel GPU computing.

### 3 GPU-ACCELERATED MESH DECIMATION

To explore hierarchical neural networks on 3D meshes, there is a need of efficient mesh decimation technique that suits deep learning for on-the-fly network reduction. The QEM algorithm [25] is effective at simplifying meshes while retaining the decimation quality. However, it applies contractions to each vertex pair iteratively with a global optimal quadric error. The implicit dependencies between the iterative contractions make this method unsuitable for parallel acceleration<sup>3</sup>. Hence, we propose an enhancement of QEM to enable parallel computing with GPUs. In our method, we do not allow inter-dependent iterative contractions. Instead, we group the vertices into multiple disjoint clusters under a reasonable compromise on the quadric error cost. We control the clustering process using expected number of vertices in the decimated mesh rather than the number of edges or facets. Due to the disjointness of vertex clusters, their contractions are independent of each other and can be executed in parallel. We provide a toy example in Fig. 2 to illustrate our procedure of vertex clustering.

In our method, we establish the vertex pairs for candidate contraction using the end-vertices of mesh geodesic edges only. To prioritize the vertex pairs that contribute to lower quadric errors, they are arranged in ascending order. Each vertex cluster is then initialized as a disjoint vertex pair in the ascending order of the candidates. We summarize our mesh simplification procedure as Algorithm 1 that reduces the number of mesh vertices to nearly a half per-iteration. To handle mesh decimation of arbitrary number of vertices, we allow the core algorithm to be iterated for flexible ( $\geq 1$ ) times. In Algorithm 1, we present the decimation method for a single mesh as the input for clarity. Our decimation function implementation processes ‘mini-batches’ of multiple meshes. We execute the vertex clustering (*lines 5–16*) on CPU while all the other operations that require heavy computations are performed on GPU. The clustering process has a time complexity of  $\mathcal{O}(|\mathcal{E}|)$ , where  $|\mathcal{E}|$  is the number of edges of the input mesh. The routine penalties, and consistency checks in mesh decimation are excluded in our method to favor runtime efficiency. We compare the runtime of QEM and the proposed decimation algorithm in Fig. B.1 of the supplementary, where our method is much faster.

In our implementation, we also record the vertex clustering information with a parameter  $VCluster$ , and the vertex

3. We summarise the QEM method in Algorithm A.1 of the supplementary where its iterative dependency is clear from *lines 7–13*.

---

#### Algorithm 1 The GPU-accelerated mesh simplification

---

**Input:** mesh  $\mathcal{T}^i=(\mathcal{V}^i, \mathcal{F}^i)$ ; number of vertices to remove  $N_r$ .

**Output:** decimated mesh  $\mathcal{T}^o=(\mathcal{V}^o, \mathcal{F}^o)$ .

- 1: establish a vertex pair  $(\mathbf{v}_i, \mathbf{v}_j)$  for each edge.
  - 2: compute the quadric cost of contracting each pair.
  - 3: sort all pairs ascendingly based on the quadrics.
  - 4: set  $n_r = 0$ , and  $p(\mathbf{v}_i) = \text{false}, \forall \mathbf{v}_i \in \mathcal{V}^i$ .
  - 5: **for** each pair  $(\mathbf{v}_i, \mathbf{v}_j)$  **do**
  - 6:   **if**  $p(\mathbf{v}_i) = \text{false}, p(\mathbf{v}_j) = \text{false},$  and  $n_r < N_r$  **then**
  - 7:     (a) initialize  $\{\mathbf{v}_i, \mathbf{v}_j\}$  as a new cluster.
  - 8:     (b) set  $n_r = n_r + 1, p(\mathbf{v}_i) = \text{true}, p(\mathbf{v}_j) = \text{true}$ .
  - 9:   **end if**
  - 10: **end for**
  - 11: **for** each pair  $(\mathbf{v}_i, \mathbf{v}_j)$  **do**
  - 12:   **if**  $p(\mathbf{v}_i) = \text{false or } p(\mathbf{v}_j) = \text{false},$  and  $n_r < N_r$  **then**
  - 13:     (a) place  $\mathbf{v}_i, \mathbf{v}_j$  to the same cluster.
  - 14:     (b) set  $p(\mathbf{v}_i) = \text{true}, p(\mathbf{v}_j) = \text{true}$ .
  - 15:   **end if**
  - 16: **end for**
  - 17: **for** each cluster  $\{\mathbf{v}_i, \mathbf{v}_j, \dots\}$  **do**
  - 18:   (a) compute the average position  $\bar{\mathbf{v}}$  of the cluster.
  - 19:   (b) contract the cluster to  $\bar{\mathbf{v}}$ .
  - 20: **end for**
  - 21: **return**
- 

mapping between input and output meshes with a parameter  $IOMap$ . They are both vectors of the same sizes as the number of vertices  $|\mathcal{V}^i|$  in the input mesh  $\mathcal{T}^i = (\mathcal{V}^i, \mathcal{F}^i)$ . Our decimation function yields those two parameters along with the decimated mesh as they are required in the computations of (un)poolings.

**(Un)poolings:** The clustering and mapping information encoded in vectors  $VCluster$  and  $IOMap$  largely facilitate the (un)pooling computations. Considering each cluster as a local region or neighborhood, common pooling operations such as ‘sum’/‘average’/‘max’/‘median’/‘weighted’ can be directly defined. We provide  $\max(\cdot)$ , and  $\text{average}(\cdot)$  poolings to down-sample the features. For unpooling, all vertices in a cluster replicate features of a representative vertex that the cluster is contracted to in the decimated mesh. Consider the input and output meshes in Fig. 2 as an example. We compute the feature of vertex ‘1’ in the decimated mesh as  $h^1 = \max(h^a, h^b, h^g)$  under max pooling, while create the features of  $\{a, b, g\}$  as  $h^a = h^b = h^g = h^1$  in unpooling. In addition to the mesh decimation and (un)poolings, we also introduce convolutional operations that are more compatible to feature learning on triangular meshes than the previous graph convolutions [15].

### 4 MESH CONVOLUTIONS

To discuss the proposed mesh convolutions, we first briefly introduce a few notions. We represent a triangular mesh as  $\mathcal{T} = (\mathcal{V}, \mathcal{F})$ , which is a tuple of vertices and facets. Each vertex has spatial coordinates  $\mathbf{x} = (x, y, z)$ , and may have additional features like texture  $\mathbf{c} = (r, g, b)$ , normal and intensity. Let the area and normal of a facet be  $A$  and  $\mathbf{n} = (n_x, n_y, n_z)$ . For a rendered mesh, we further denote the texture size of a facet as  $K \times 3$ , where  $K$  relates to the texture resolution and ‘3’ indicates the  $(r, g, b)$  values.

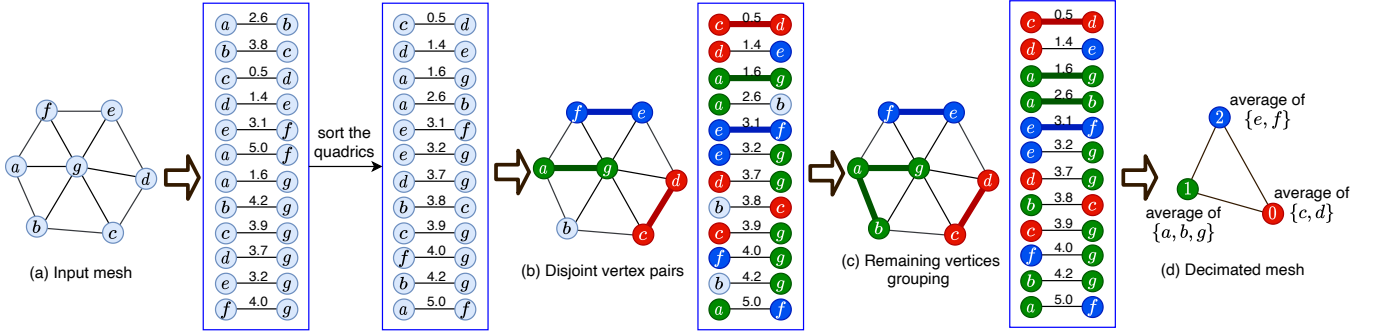


Fig. 2. Illustration of the vertex clustering process. (a) An input mesh with twelve edges (vertex pairs). We sort the vertex pairs in ascending order according to their quadric errors. (b) Then, we initialize the clusters as  $\{c, d\}, \{a, g\}, \{e, f\}$  using the disjoint vertex pairs  $(c, d), (a, g), (e, f)$  - shown by red, green and blue. (c) We group the remaining vertex  $b$  to the vertex cluster  $\{a, g\}$  because  $(a, b)$  holds the smallest quadric error among all pairs containing  $b$ , i.e.  $(a, b), (b, g), (b, c)$ . Finally, the vertex clusters become  $\{c, d\}, \{a, b, g\}, \{e, f\}$ . (d) We construct the decimated mesh by applying vertex contraction to each cluster. The target position of contraction is computed as the average location of all vertices in the cluster.

We allow  $K$  to vary according to the area of facets. This is elaborated further in § 4.3.

#### 4.1 Facet2vertex Convolution

We compute features of each vertex by aggregating context information from adjacent facets, rather than neighboring vertices. This avoids transforming a mesh into a graph for context propagation. The facet normal is directional data residing on the surface of a unit sphere. We define our kernel by associating filter weights to different positions on the sphere, while the kernel size relates to the number of different positions. Typically, normals of real-world meshes, especially the indoor meshes, are distributed as distinctive pattern clusters on the unit sphere, resulting from human construction preferences<sup>4</sup>. We exploit the von Mises-Fisher (vMF) mixture [37] to cluster the normals, and associate each filter of our kernel to a vMF component.

Let the total number of components in the vMF mixture be  $T$ , their mean directions be  $\{\mu_t\}$ , and their concentration parameters be  $\kappa = 1/\tau$ . Based on its normal  $\mathbf{n}_i$ , we compute the fuzzy coefficients  $\{\pi_{it}\}$  of each facet  $\mathbf{f}_i$  as

$$\pi_{it} = \frac{\exp(\kappa \mu_t^\top \mathbf{n}_i)}{\sum_{s=1}^T \exp(\kappa \mu_s^\top \mathbf{n}_i)}. \quad (1)$$

We fix the parameter ‘ $\tau$ ’ as 0.1 which results in ‘ $\kappa$ ’ to be 10. This setting is motivated by the definition of contrastive loss in SimCLR [81]. Softmax function is a straightforward choice to normalize those fuzzy coefficients. We keep the mean directions  $\{\mu_t\}$  as learnable parameters of the vMF mixture. They are initialized randomly and trained together with the filter weights of the network.

Following previous works [18], [82], we define the facet2vertex convolution in a depth-wise separable manner to save computations. Let the filter weights in the kernel be  $\{w_t\}$ , the adjacent facets of vertex  $\mathbf{v}$  be  $\mathcal{N}(\mathbf{v})$ , and the associated features of those facets be  $\{h_i^f | \mathbf{f}_i \in \mathcal{N}(\mathbf{v})\}$ . The feature of vertex  $\mathbf{v}$  is computed as

$$g^v = \frac{1}{\mathcal{N}(\mathbf{v})} \sum_{\mathbf{f}_i \in \mathcal{N}(\mathbf{v})} \left( \sum_{t=1}^T \pi_{it} w_t \right) h_i^f, \quad (2)$$

$$h^v = \text{activation}(g^v). \quad (3)$$

4. To illustrate, we provide an example of mesh normal distribution of S3DIS [20] in Fig. C.1 of the supplementary.

We use ReLU [83] as the activation function. The bias term in feature computation is omitted for simplicity. Considering that we model the fuzzy coefficients based on facet normals, the resulting facet2vertex convolution is scale and translation invariant but not rotation invariant.

#### 4.2 Vertex2facet Convolution

We aggregate features of each facet from its vertices. The vertex2facet convolution exploits depth-wise separable strategy as well. Let  $\{\mathbf{v}_1, \mathbf{v}_2, \mathbf{v}_3\}$  be the three vertices of triangular facet  $\mathbf{f}$ , and the features of those vertices be  $\{h_1^v, h_2^v, h_3^v\}$ . We define a kernel composed of three filters, which are associated to the three vertices and have filter weights  $\{w_1, w_2, w_3\}$ . We compute the feature of facet  $\mathbf{f}$  as

$$g^f = \sum_{k=1}^3 w_k h_k^v. \quad (4)$$

The Barycentric interpolation in [38] is no longer retained in the vertex2facet convolution as it makes minor contributions to the feature extraction but requires additional computations. Point cloud convolutions propagate local information from points to points [18], [31], [59]. We induce a vertex2vertex convolution to achieve similar propagation by combining the vertex2facet and facet2vertex convolutions. Figure 3 illustrates the notion of facet2vertex, vertex2facet, vertex2vertex, and facet2facet convolutions.

#### 4.3 Facet2facet Convolution

The facet2facet convolution is applicable to textured meshes. We calculate the features of each facet based on the textures of all points on the facet. Let  $\{\mathbf{h}_k^f \in \mathbb{R}^{C_i}\}$  be the input features of all points on a facet, and the associated Barycentric coordinates of each point be  $\{\xi_k = [\xi_{k1}, \xi_{k2}, \xi_{k3}]^\top | \xi_{k1} + \xi_{k2} + \xi_{k3} = 1, \xi_{k1}, \xi_{k2}, \xi_{k3} \geq 0\}$ . A facet of texture resolution  $K$  leads to  $|\{\mathbf{h}_k^f\}| = |\{\xi_k\}| = K$ . We define a convolutional kernel as  $\{\mathbf{w}_1, \mathbf{w}_2, \mathbf{w}_3 \in \mathbb{R}^{C_i}\}$ . The fuzzy scheme [44] is incorporated to facet2facet convolution using Barycentric coordinates. Finally, we compute the feature of facet  $\mathbf{f}$  as

$$g^f = \frac{1}{K} \sum_k (\xi_{k1} \mathbf{w}_1 + \xi_{k2} \mathbf{w}_2 + \xi_{k3} \mathbf{w}_3)^\top \mathbf{h}_k^f. \quad (5)$$

We note that the facet2facet convolution is only required at the first convolution layer for extracting texture features



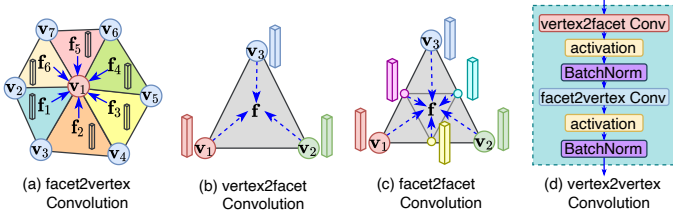


Fig. 3. Mesh convolutions introduced in Picasso. (a) The facet2vertex convolution propagates features from the adjacent facets of a vertex to the vertex itself. (b) The vertex2facet convolution computes the features of a facet based on its three vertices. (c) The facet2facet convolution calculates features of a rendered facet based on the vertices and interpolated points in the facet. For simplicity, we show only three interpolated points on the rendered facet. It corresponds to a setting of  $\gamma = 1$  and  $K = 6$  following Eq. (6). (d) The vertex2vertex convolution is composed of a vertex2facet convolution followed by a facet2vertex convolution. We apply batch normalization to both vertex and facet features.

from the raw mesh input. We prepare fine textures for the mesh data using Barycentric interpolation [84] in the experiments. The texture resolution  $K$  of a facet  $\mathbf{f}$  is determined by its area  $A$ , and it is computed as

$$K = \frac{(\gamma + 1)(\gamma + 2)}{2}, \text{ where } \gamma = \left\lfloor \frac{\alpha(A - A_{\min})}{A_{\max} - A_{\min}} \right\rfloor + \beta. \quad (6)$$

We use  $\gamma$  to represent the number of interpolated points on each edge. In Eq. (6),  $A_{\min}$ ,  $A_{\max}$  are the minimum and maximum facet areas of the mesh, while  $\alpha, \beta \in \mathbb{Z}_{\geq 0}$  are hyperparameters. For all settings in the group of  $\alpha=0$ , we let the texture resolution  $K$  to be constant across all mesh facets. One special case in this group is when the mesh is provided with vertex colors but its facets are not rendered. In that case,  $K$  correlates to  $(\alpha, \beta)=(0, 1)$  and takes value  $K = 3$ . In this situation, we can alternatively fulfill the facet2facet convolution with a simple  $1 \times 1$  convolution, by formulating the texture features of each facet as a concatenation of its vertex colors, *i.e.*  $[c_1, c_2, c_3]$ .

#### 4.4 Geometric Facet Features

Let us denote the coordinates of facet vertices by  $\mathbf{x}_1, \mathbf{x}_2, \mathbf{x}_3$ , the edge lengths of the facet as  $\ell = (\ell_1, \ell_2, \ell_3)$  and the facet normals as  $\mathbf{n}$ . We compute inner angles of a facet  $\boldsymbol{\theta} = (\theta_1, \theta_2, \theta_3)$  as

$$\begin{aligned} \theta_1 &= \frac{\langle \mathbf{x}_2 - \mathbf{x}_1, \mathbf{x}_3 - \mathbf{x}_1 \rangle}{\ell_1 \ell_3}, \\ \theta_2 &= \frac{\langle \mathbf{x}_1 - \mathbf{x}_2, \mathbf{x}_3 - \mathbf{x}_2 \rangle}{\ell_1 \ell_2}, \\ \theta_3 &= \frac{\langle \mathbf{x}_1 - \mathbf{x}_3, \mathbf{x}_2 - \mathbf{x}_3 \rangle}{\ell_2 \ell_3}. \end{aligned} \quad (7)$$

We form the input feature representation composed of mesh facet geometry as  $[\ell, \boldsymbol{\theta}, \mathbf{n}]$  for shapes. For real-world surface data with aligned gravitational-axis (*e.g.* the  $z$ -axis), we form their facet geometrics as  $[\ell, \boldsymbol{\theta}, \mathbf{n}, \mathbf{h}]$ , where  $\mathbf{h}$  concatenates the heights of the three vertices, *e.g.*  $\mathbf{h} = [z_1, z_2, z_3]$ . The use of our facet geometric representation is empirically supported in § 8.2. For network training, we allow the direction of facet normals to be arbitrary (*i.e.*  $\pm \mathbf{n}$ ). This randomness plays an effective role of data augmentation. We note that the standard input features to our network in § 6 include

both facet geometrics and facet textures. However, when the mesh is not textured, we employ only facet geometrics as the input features.

## 5 PICASSO OVERVIEW

We combine the operations proposed in this work for mesh processing with our previously proposed operations for 3D point cloud processing in [18], [44] into *Picasso*. The previous point cloud operations are improved to handle point clouds of heterogeneous sizes in addition to homogeneous arrays. This improvement has led to seamless integration of our mesh and point cloud operations. Through Picasso, we make geometric deep learning over 3D data accessible to the broader research community. We allow easy integration of the contributed modular operations in 3D domain with the modern deep learning blocks/layers such as ResNet [6], DenseNet [85], Inception [86] etc. Figure 4 provides an overview of the major modules in Picasso. To differentiate this article’s contribution from [18], [44], the figure colorizes only the novel operations introduced in this work. These include CUDA-accelerated mesh decimation, pooling, unpooling, and different mesh convolutions. We additionally incorporate a module for GPU-based voxelization of point clouds and meshes in Picasso. The module allows mesh decimation with voxelized vertex clustering to be performed on-the-fly. Picasso is supported by both Tensorflow [34] and Pytorch [35] for different user preferences. We release the code at <https://github.com/EnyaHermite/Picasso>.

To build a deep convolutional block for feature learning in Picasso, multiple vertex2vertex convolutions can be cascaded within a network layer of the same mesh resolution, similar to the usage of CNN kernels. In Fig. 1(left), an example is shown for constructing a simple hierarchical mesh network using mesh convolutions and poolings. The example network is sequentially composed of an initial convolutional layer, a max pooling layer, one convolutional block, a global pooling and an arbitrary classifier. Assume the network uses batch size 3 for training. Let  $\mathcal{T}_1=(\mathcal{V}_1, \mathcal{F}_1)$ ,  $\mathcal{T}_2=(\mathcal{V}_2, \mathcal{F}_2)$ ,  $\mathcal{T}_3=(\mathcal{V}_3, \mathcal{F}_3)$  be different shapes in a batch, and  $\mathcal{H}_1^0, \mathcal{H}_2^0, \mathcal{H}_3^0$  be the input features of  $\mathcal{T}_1, \mathcal{T}_2, \mathcal{T}_3$ , respectively. The standard input features  $\mathcal{H}^0$  of a mesh comprise both facet geometrics  $\mathcal{H}_G^0$  and facet textures  $\mathcal{H}_C^0$ . As the shape meshes provided in the example do not contain textures, the input features are simplified to  $\mathcal{H}^0=\mathcal{H}_G^0$ . In Picasso, we customize the network to accept multiple meshes via concatenation. Therefore, the shapes in the batch input are represented as a tuple of  $(\mathbf{V}, \mathbf{F}, \mathbf{H}^0)$ , where

$$\mathbf{V} = \begin{bmatrix} \mathcal{V}_1 \\ \mathcal{V}_2 \\ \mathcal{V}_3 \end{bmatrix}, \mathbf{F} = \begin{bmatrix} \mathcal{F}_1 + 0 \\ \mathcal{F}_2 + |\mathcal{V}_1| \\ \mathcal{F}_3 + |\mathcal{V}_1| + |\mathcal{V}_2| \end{bmatrix}, \mathbf{H}^0 = \mathbf{H}_G^0 = \begin{bmatrix} \mathcal{H}_{G,1}^0 \\ \mathcal{H}_{G,2}^0 \\ \mathcal{H}_{G,3}^0 \end{bmatrix}. \quad (8)$$

For facet concatenations in  $\mathbf{F}$ , we follow 0-indexing convention. Without textures, the initial layer of the shape example consists of a  $1 \times 1$  convolution followed by a facet2vertex convolution. However, the standard initial layer covers both geometrics  $\mathbf{H}_G^0$  and textures  $\mathbf{H}_C^0$  as input features. We show its configurations in Fig. 1(right). To pool the features, the mesh has to be decimated first such that the pooling operation can proceed. We exploit max pooling in the example, while the convolutional block comprises two

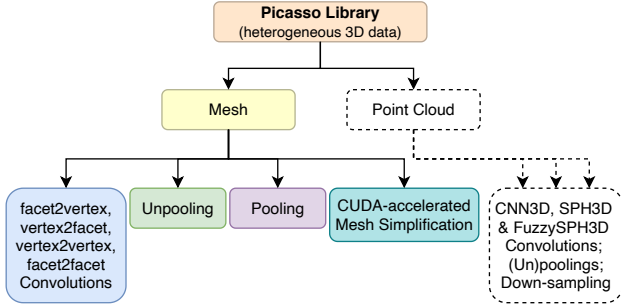


Fig. 4. Overview of the major deep learning modules included in Picasso. We only colorize the novel modules proposed in this work. Picasso allows feature learning for both heterogeneous 3D mesh and heterogeneous 3D point cloud.

vertex2vertex convolutions. Global pooling induces a single representation for each sample such that the final classification can be applied. We give a basic example network in Fig. 1 to provide a clear overview of Picasso. Next, we build our proposed network that also offers a more advanced example of using the Picasso modules.

## 6 PICASSONET-II

Besides extending Picasso beyond the preliminary work in [38], this article also considerably enhances PicassoNet [38] to introduce a more effective network PicassoNet-II. Compared to [38], PicassoNet-II is deeper yet faster for geometric feature learning over 3D meshes. We show its configuration in the Fig. 5(top), which also includes a decoder part (boxed) for dense parsing. For classification, the decoder is replaced with an average global pooling layer. PicassoNet-II takes *intact* meshes rather than mesh crops as input samples. We apply strided mesh decimation by specifying the expected vertex size using a stride parameter. This removes the constraint of fixing vertex sizes across different samples.

As meshes are not always guaranteed to form a connected graph (*e.g.* after decimation), PicassoNet-II exploits point cloud convolution to extract features across disconnected components of the mesh, similar to [38]. The Euclidean neighborhood in point cloud convolution allows larger context to be established such that feature learning can go beyond geodesic connections. Whereas the previous methods [15], [38] explored Euclidean neighborhood extensively in every network layer regardless of the mesh resolution, PicassoNet-II employs it only at the coarse layers of low mesh resolutions. We validate in § 8.3 that point cloud convolution in the Euclidean domain is unnecessary for high-resolution layers since the meshes are already well-connected. Selective application of convolutions in PicassoNet-II results in considerable computational gain without compromising performance.

Our network uses range search [87] to construct the neighborhood, and fuzzy spherical convolution [44] to learn features in the Euclidean domain. It exploits two types of encoder blocks to extract features from the meshes of different resolutions. One is *mesh* encoder block, which comprises a repetitive building unit that uses only two vertex2vertex convolutions. The other is *dual* encoder block, whose repetitive building unit is two vertex2vertex convolutions accompanied by one spherical convolution. We use identical feature channels for mesh and point cloud convolutions

in the dual encoder blocks. PicassoNet-II employs mesh encoder blocks in high-resolution layers and dual encoder blocks in the low-resolution layers. Our network inherits the primary building units of PicassoNet. However, it applies skip connections to every building unit of the encoder block. Besides, it leverages the concatenation-style skip connection of DenseNet [85], instead of the addition-style skip connection of ResNet [6]<sup>5</sup>. Figure 5(bottom) depicts the key blocks of PicassoNet-II, including its initial convolution, mesh and dual encoder blocks, as well as the decoder blocks. We employ max mesh pooling to down-sample the network features.

PicassoNet-II takes facet textures and geometrics as input features. This differs from PicassoNet [38], which follows point cloud networks in expecting vertex coordinates and colors as input features. To propagate the input features from facet to vertex, we build the initial layer of PicassoNet-II using a  $1 \times 1$  convolution with a parallel facet2facet convolution, followed by a feature fusion of addition ‘+’ and a facet2vertex convolution. The  $1 \times 1$  convolution is used for extracting geometric features while the facet2facet convolution is for learning texture representations. We adopt the ‘+’ feature fusion for its simplicity. It can be replaced by *e.g.* attentional fusion [73] for better performance at the expense of higher computational cost. For decoder, we use the  $1 \times 1$  convolutions and mesh unpooling of PicassoNet [38] to upsample features. PicassoNet-II applies batch normalization to all of its modular convolutions.

The proposed network repeats the building unit of its dual encoder blocks  $m=4$  times, resulting in a deeper network than PicassoNet. For classification, we replace the single  $1 \times 1$  convolution for final predictions in dense parsing with two fully connected (FC) layers. Also, a dropout [88] of rate 0.2 is applied after the first FC layer.

## 7 EXPERIMENTS

We establish the effectiveness of PicassoNet-II by evaluating it for (i) shape analysis with synthetic meshes and (ii) semantic scene parsing using real-world meshes. We use the ShapeNetCore [39] dataset, along with SHREC [40], CUBE [1], COSEG [41], HUMAM [42] and FAUST [43] for shape analysis. For real-world scene parsing, we employ the large-scale datasets S3DIS [20] and ScanNet [3]. Each dataset is discussed with its related experiments. For all shape analysis experiments in § 7.1, we normalize the scales of all shape meshes, but keep the original scales of real-world scene surfaces in § 7.2. This is because scale information is more important for real-world scenes. We employ the proposed facet geometrics  $[\ell, \theta, \mathbf{n}]$  as default input features for synthetic shapes, and  $[\ell, \theta, \mathbf{n}, \mathbf{h}]$  as default geometric features for the real-world data. Additionally, real-world data also provides facet textures for experiments.

**Data Augmentation:** We apply standard geometric transformations, *e.g.* random flipping, scaling and shifting to the mesh vertices. We perform random rotations along the gravitational axis for aligned data in ShapeNetCore, ScanNet and S3DIS, and free data rotation along all axes

<sup>5</sup> The DenseNet-style connection is slightly less efficient but usually produces 0.5% higher results.

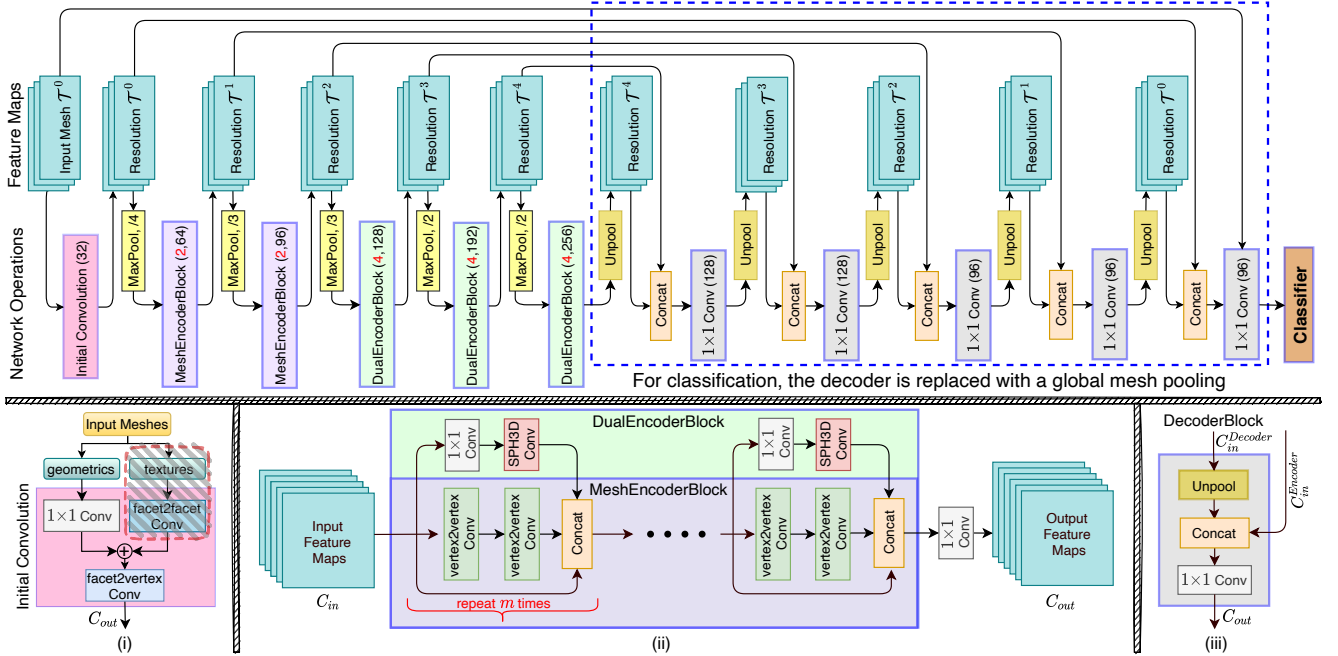


Fig. 5. PicassoNet-II for large-scale semantic parsing of complete scenes (top), and its convolution blocks (bottom). The network consists of six mesh resolutions including the input  $\mathcal{T}^0 \sim \mathcal{T}^5$ . The output channels are respectively 32, 64, 96, 128, 192, 256 in the encoder and 128, 128, 96, 96, 96 in the decoder. The pooling strides are 4, 3, 3, 2, 2, which can be different for shape analysis. The figure depicts predicting semantics of mesh vertices, a vertex2facet convolution can be inserted before the final classifier for facet-based predictions. For classification, the decoder is replaced by a global mesh pooling. The bottom row shows (i) the ‘Initial Convolution’ which propagates input features from facet to vertex; (ii) the ‘MeshEncoderBlock’ that is exploited in high-resolution layers for feature extraction, along the ‘DualEncoderBlock’ that applies to low-resolution layers such that feature extraction can go beyond disconnected components of the mesh, and (iii) the ‘DecoderBlock’ for feature unsampling from low-resolution meshes to high-resolution meshes. In the ‘Initial Convolution’, the facet2facet convolution is not applicable if textures are not provided. We apply ‘MeshEncoderBlock’ to  $\mathcal{T}^1, \mathcal{T}^2$  and ‘DualEncoderBlock’ to  $\mathcal{T}^3, \mathcal{T}^4, \mathcal{T}^5$ . They repeat  $m=2$  and  $m=4$  times, respectively.

for other datasets. We also randomly drop the vertices and facets of meshes to obtain more training data. When textures are available, we apply color shifting, jittering, and color contrast to augment the data further, following [28].

**Network Configuration:** PicassoNet-II contains 6 hierarchical layers of mesh resolutions from  $\mathcal{T}^0$  to  $\mathcal{T}^5$  that use mesh decimation. We set different decimation strides for different datasets, discussed in the respective experiments. Our network uses dual encoder blocks only at coarse resolutions  $\mathcal{T}^3, \mathcal{T}^4, \mathcal{T}^5$ . The range search radii for point-based convolutions of  $\mathcal{T}^3$  to  $\mathcal{T}^5$  are 0.2, 0.4, 0.8, respectively. We train the network with Adam Optimizer [89] and exponential decay. The initial learning rate is set to 0.001, with 0.5 decay rate.

### 7.1 Shape Analysis

We evaluate our network performance on shape classification and facet labelling tasks using synthetic data. The input meshes are decimated with strides 1, 3, 2, 2, 2, respectively on ShapeNetCore and FAUST, while 1, 1.5, 1.5, 1.5, 1.5 on the other datasets due to their limited number of input vertices. Here, the first stride ‘1’ indicates the  $\mathcal{T}^0$  is not decimated and it is identical to  $\mathcal{T}^1$ . Therefore, the first pooling operation in PicassoNet-II is not applied. We train the network using batch size 6 for FAUST, 32 for ShapeNetCore, and 64 for others. A weight decay of  $10^{-5}$  is applied to all datasets other than ShapeNetCore for their limited training samples.

#### 7.1.1 Classification

**ShapeNetCore:** The ShapeNetCore dataset [39] is a large-scale and information-rich repository of 3D models collected from online resources. It contains around 51,000 shapes

of 55 common objects. We follow the original standard split to evaluate the performance of PicassoNet-II for shape classification. In specific, the split specifies 80% samples for training and 20% for testing. Table 1 shows that our network outperform the sparse Residual network of PointContrast [92] by 2.5%. This indicates the desirability of processing mesh data with PicassoNet-II for shape analysis. We prepare the input meshes to our network by uniformly sampling 3,000 points on the raw mesh, and triangulating them using the algorithm provided by [93]. We note that these meshes are not ideal and actual watertight meshes should result in even better performance of our network.

**SHREC:** The SHREC dataset [1], [40] contains 600 watertight meshes from 30 classes, with 20 samples in each class. Shape classification is defined on split 16 and 10 of the dataset. The split number here indicates the number of training samples per class. Following the setup in [1], we report the average results over three randomly generated sets. Table 1 shows excellent performance of PicassoNet-II.

**CUBE:** The CUBE Engraving dataset [1] includes 22 object categories with 200 mesh samples per class. Those samples are created by insetting the MPEG-7 binary shapes [94] into random locations of a cube. Each cube consists of about 250 vertices and 500 facets. Table 1 shows that our network achieves 100% accuracy on this dataset.

#### 7.1.2 Semantic Labelling

**COSEG:** The COSEG dataset [41] defines semantic labelling tasks over three independent categories, *i.e.* *aliens*, *chairs* and *vases*. The alien category contains 169 training samples, 29



TABLE 1  
Shape analysis performance of our network on the synthetic datasets.

| Method                | Classification |              |              |              | Semantic Labelling |             |             |             | Correspondence |
|-----------------------|----------------|--------------|--------------|--------------|--------------------|-------------|-------------|-------------|----------------|
|                       | ShapeNetCore   | SHREC        |              | CUBE         | COSEG              |             |             | HUMAN       | FAUST          |
|                       |                | Split 16     | Split 10     |              | aliens             | chairs      | vases       |             |                |
| GI [90]               | -              | 96.6         | 88.6         | -            | -                  | -           | -           | -           | -              |
| GWCNN [91]            | -              | 96.6         | 90.3         | -            | -                  | -           | -           | -           | -              |
| PointNet++ [32]       | -              | -            | -            | 64.3         | -                  | -           | -           | -           | -              |
| MeshCNN [1]           | -              | 98.6         | 91.0         | 92.2         | 96.3               | 93.0        | 92.4        | 85.4        | -              |
| PD-MeshNet [77]       | -              | 99.7         | 99.1         | 94.4         | 98.2               | 97.2        | 95.4        | 85.6        | -              |
| GCNN [75]             | -              | -            | -            | -            | -                  | -           | -           | -           | 65.4           |
| ACNN [21]             | -              | -            | -            | -            | -                  | -           | -           | -           | 63.0           |
| MoNet [22]            | -              | -            | -            | -            | -                  | -           | -           | -           | 90.0           |
| PointContrast [22]    | 85.1           | -            | -            | -            | -                  | -           | -           | -           | -              |
| PicassoNet-II (Prop.) | <b>87.6</b>    | <b>100.0</b> | <b>100.0</b> | <b>100.0</b> | <b>98.8</b>        | <b>99.6</b> | <b>96.0</b> | <b>91.4</b> | <b>100.0</b>   |

test samples and 4 part labels. The chair category contains 337 training samples, 60 test samples and 3 part labels. The vase category contains 252 training samples, 45 test samples and 4 part labels. We follow [77] and evaluate our network under semantic facet labelling. Table 1 reports the consistent superior performance of PicassoNet-II.

**HUMAN:** The HUMAN dataset [42] defines semantic facet labelling as segmenting the human body into 8 parts, which include *head, hand, forearm, upperarm, body, thigh, leg* and *foot*. It contains 381 training samples and 18 test samples. Each mesh sample is composed of 750 vertices and 1,500 facets. Table 1 suggests that the segmentation result of PicassoNet-II outperforms the previous methods by a large margin.

### 7.1.3 3D Manifold Correspondence

**FAUST:** The FAUST dataset [43] is widely used for correspondence matching of 3D manifold meshes [21], [22], [75]. It consists of 10 different subjects with 10 different poses each, resulting in 100 watertight meshes with exact ground-truth correspondence. Each shape is represented as a mesh with 6,890 vertices and 13,776 facets. The convention is to utilize the first pose of the first subject (i.e. the zeroth scan '000') as the reference, the first 80 shapes for training and the rest 20 shapes for testing. We follow MoNet [22] and formulate the correspondence task as a multi-class labelling problem. Similar to its configurations in semantic labelling, the proposed network accomplishes this correspondence labelling with softmax function. In specific, the number of classes is defined as 6,890, i.e. the number of vertices in the reference mesh. We report the matching accuracy of different methods for correspondences without geodesic error in Table 1. Feature representation of our network achieves 100% accuracy, which is considerably better than other methods.

## 7.2 Real-world Datasets

Real-world scene surfaces have heterogeneous vertex and facet sizes, and varying scales. We decimate the input meshes using strides 4, 3, 3, 2, 2, respectively, to construct network layers of mesh resolutions from  $\mathcal{T}^1$  to  $\mathcal{T}^5$ . The network is trained with batch size 16.

**S3DIS.** The Stanford 3D Indoor Spaces (S3DIS) dataset [20] is a large-scale real-world dataset. It has sparse 3D meshes and dense 3D point clouds of 6 large-scale indoor areas. The data was collected, using the Matterport scanner, from three different buildings in Stanford University campus. The

semantic labelling task on this dataset is defined to classify 13 classes, namely *ceiling, floor, wall, beam, column, window, door, table, chair, sofa, bookcase, board, and clutter*. We follow the standard training/testing protocol where Area 5 is used as the test set and the remaining 5 Areas as the training set [59], [68], [95], [96], [98]. Performance of each method is evaluated for Overall Accuracy (OA), mean Accuracy of all classes (mAcc), Intersection Over Union of each class (IoU) and their average over all classes (i.e. mIoU). mIoU is normally considered the most reliable among these metrics.

DCM-Net [15] prepared its training meshes and labels based on the original meshes with over-tessellation and interpolation. In contrast, we generate the scene meshes by triangulating the labelled point cloud provided in the dataset. In specific, we voxelize the raw point cloud using a voxel size of 0.03 (3cm), and triangulate them into meshes using the algorithm from [93]. We guarantee all of the created meshes to be *edge-manifold*. In this experiment, we utilize the default facet geometrics together with rendered facets of texture resolutions determined by  $(\alpha, \beta) = (3, 3)$  as input features to PicassoNet-II. We train and test the network using complete scenes as input samples. It can be noticed from Table 2 that our method significantly outperforms the previous methods. The average inference time of PicassoNet-II is 60ms across the 68 (voxelized) test samples in Area 5, using a single NVIDIA 3090 GPU. The final results reported in Table 2 are computed on the original point cloud. We transfer the voxelized predictions to dense predictions using nearest neighborhood search.

**ScanNet.** The ScanNet dataset [3] comprises reconstructed room meshes from RGB-D video frames, and has rich annotations for semantic vertex labelling. It includes 1,613 meshes in total, among which 1,213 scenes are used for training and 300 scenes for validation. We ignore the 100 test samples in our experiment as their labels are unavailable. The dataset contains 40 class labels, while 20 are recommended for performance evaluation. We train and test our network with complete scene samples.

Our network takes voxelized mesh of grid size 2cm as the input. Yet, for better performance, we generate those inputs by voxelizing the raw meshes on-the-fly after data augmentation has been applied. This results in PicassoNet-II unable to benefit from rendered textures since on-the-fly rendering of large-scale data is computationally intractable. We therefore use only vertex colors to form the fact textures. Our results on the validation set of ScanNet is 71.9%, which

TABLE 2

Performance of PicassoNet-II on the fifth fold (Area 5) of S3DIS dataset. The results are obtained by taking each *complete* scene as input. Our network outperforms the previous best approaches, MinkowskiNet and KPConv, by a significant margin.

| Method                | OA          | mAcc        | mIoU        | ceiling     | floor       | wall        | beam | column      | window      | door        | table       | chair       | sofa        | bookcase    | board       | clutter     |
|-----------------------|-------------|-------------|-------------|-------------|-------------|-------------|------|-------------|-------------|-------------|-------------|-------------|-------------|-------------|-------------|-------------|
| PointNet [59]         | -           | 49.0        | 41.1        | 88.8        | 97.3        | 69.8        | 0.1  | 3.9         | 46.3        | 10.8        | 58.9        | 52.6        | 5.9         | 40.3        | 26.4        | 33.2        |
| SEGCloud [95]         | -           | 57.4        | 48.9        | 90.1        | 96.1        | 69.9        | 0.0  | 18.4        | 38.4        | 23.1        | 70.4        | 75.9        | 40.9        | 58.4        | 13.0        | 41.6        |
| Tangent-Conv [57]     | 82.5        | 62.2        | 52.8        | -           | -           | -           | -    | -           | -           | -           | -           | -           | -           | -           | -           | -           |
| SPG [96]              | 86.4        | 66.5        | 58.0        | 89.4        | 96.9        | 78.1        | 0.0  | <b>42.8</b> | 48.9        | 61.6        | 75.4        | 84.7        | 52.6        | 69.8        | 2.1         | 52.2        |
| PointCNN [68]         | 85.9        | 63.9        | 57.3        | 92.3        | 98.2        | 79.4        | 0.0  | 17.6        | 22.8        | 62.1        | 74.4        | 80.6        | 31.7        | 66.7        | 62.1        | 56.7        |
| SSP+SPG [97]          | 87.9        | 68.2        | 61.7        | -           | -           | -           | -    | -           | -           | -           | -           | -           | -           | -           | -           | -           |
| GACNet [69]           | 87.8        | -           | 62.9        | 92.3        | 98.3        | 81.9        | 0.0  | 20.4        | 59.1        | 40.9        | 78.5        | 85.8        | 61.7        | 70.8        | 74.7        | 52.8        |
| SPH3D-GCN [18]        | 87.7        | 65.9        | 59.5        | 93.3        | 97.1        | 81.1        | 0.0  | 33.2        | 45.8        | 43.8        | 79.7        | 86.9        | 33.2        | 71.5        | 54.1        | 53.7        |
| SegGCN [44]           | 88.2        | 70.4        | 63.6        | 93.7        | <b>98.6</b> | 80.6        | 0.0  | 28.5        | 42.6        | <b>74.5</b> | 80.9        | 88.7        | 69.0        | 71.3        | 44.4        | 54.3        |
| MinkowskiNet [28]     | -           | 71.7        | 65.3        | -           | -           | -           | -    | -           | -           | -           | -           | -           | -           | -           | -           | -           |
| KPConv [29]           | -           | 72.8        | 67.1        | 92.8        | 97.3        | 82.4        | 0.0  | 23.9        | 58.0        | 69.0        | 81.5        | <b>91.0</b> | <b>75.4</b> | <b>75.3</b> | 66.7        | 58.9        |
| DCM-Net [15]          | -           | 71.2        | 64.0        | 92.1        | 96.8        | 78.6        | 0.0  | 21.6        | <b>61.7</b> | 54.6        | 78.9        | 88.7        | 68.1        | 72.3        | 66.5        | 52.4        |
| PicassoNet-II (Prop.) | <b>90.4</b> | <b>75.7</b> | <b>69.8</b> | <b>94.4</b> | <b>98.1</b> | <b>85.1</b> | 0.0  | 33.8        | 59.5        | 80.9        | <b>82.8</b> | 90.0        | 79.3        | 74.9        | <b>70.3</b> | <b>58.1</b> |

TABLE 3

Semantic vertex labelling results on the test set of ScanNet.

| Method                      | mIoU        | floor       | wall        | chair       | sofa        | table       | door        | cab         | bed         | desk        | toil        | sink        | wind        | pic         | bkshf       | curt        | show        | cntr        | fridg       | bath        | other       |
|-----------------------------|-------------|-------------|-------------|-------------|-------------|-------------|-------------|-------------|-------------|-------------|-------------|-------------|-------------|-------------|-------------|-------------|-------------|-------------|-------------|-------------|-------------|
| SPLATNET <sub>3D</sub> [33] | 39.3        | 92.7        | 69.9        | 65.6        | 51.0        | 38.3        | 19.7        | 31.1        | 51.1        | 32.8        | 59.3        | 27.1        | 26.7        | 0.0         | 60.6        | 40.5        | 24.9        | 24.5        | 0.1         | 47.2        | 22.7        |
| Tangent-Conv [57]           | 43.8        | 91.8        | 63.3        | 64.5        | 56.2        | 42.7        | 27.9        | 36.9        | 64.6        | 28.2        | 61.9        | 48.7        | 35.2        | 14.7        | 47.4        | 25.8        | 29.4        | 35.3        | 28.3        | 43.7        | 29.8        |
| PointCNN [68]               | 45.8        | 94.4        | 70.9        | 71.5        | 54.5        | 45.6        | 31.9        | 32.1        | 61.1        | 32.8        | 75.5        | 48.4        | 47.5        | 16.4        | 35.6        | 37.6        | 22.9        | 29.9        | 21.6        | 57.7        | 28.5        |
| PointConv [31]              | 55.6        | 94.4        | 76.2        | 73.9        | 63.9        | 50.5        | 44.5        | 47.2        | 64.0        | 41.8        | 82.7        | 54.0        | 51.5        | 18.5        | 57.4        | 43.3        | 57.5        | 43.0        | 46.4        | 63.6        | 37.2        |
| SPH3D-GCN [18]              | 61.0        | 93.5        | 77.3        | 79.2        | 70.5        | 54.9        | 50.7        | 53.2        | 77.2        | 57.0        | 85.9        | 60.2        | 53.4        | 4.6         | 48.9        | 64.3        | 70.2        | 40.4        | 51.0        | 85.8        | 41.4        |
| KPConv [29]                 | 68.4        | 93.5        | 81.9        | 81.4        | 78.5        | 61.4        | 59.4        | 64.7        | 75.8        | 60.5        | 88.2        | 69.0        | 63.2        | 18.1        | 78.4        | 77.2        | 80.5        | 47.3        | 58.7        | 84.7        | 45.0        |
| SegGCN [44]                 | 58.9        | 93.6        | 77.1        | 78.9        | 70.0        | 56.3        | 48.4        | 51.4        | 73.1        | 57.3        | 87.4        | 59.4        | 49.3        | 6.1         | 53.9        | 46.7        | 50.7        | 44.8        | 50.1        | 83.3        | 39.6        |
| MinkowskiNet [28]           | <b>73.6</b> | 95.1        | <b>85.2</b> | <b>84.0</b> | 77.2        | <b>68.3</b> | <b>64.3</b> | 70.9        | <b>81.8</b> | <b>66.0</b> | 87.4        | 67.5        | <b>72.7</b> | 28.6        | <b>83.2</b> | <b>85.3</b> | <b>89.3</b> | <b>52.1</b> | <b>73.1</b> | <b>85.9</b> | <b>54.4</b> |
| DCM-Net [15]                | 65.8        | 94.1        | 80.3        | 81.3        | 72.7        | 56.8        | 52.4        | 61.9        | 70.2        | 49.4        | 82.6        | 67.5        | 63.7        | <b>29.8</b> | 80.6        | 69.3        | 82.1        | 46.8        | 51.0        | 77.8        | 44.9        |
| PicassoNet-II (Prop.)       | 69.6        | <b>95.6</b> | 84.8        | 83.7        | <b>79.9</b> | 61.9        | 61.5        | <b>70.9</b> | 79.0        | 54.3        | <b>90.8</b> | <b>70.3</b> | 70.0        | 25.0        | 78.7        | 81.5        | 79.0        | 45.9        | 55.1        | 70.4        | 52.9        |

is 3.6% higher than DCM-Net and is very competitive to the 72.2% of the top performer MinkowskiNet. MinkowskiNet has 29.8M training parameters [92], while our network produces similar results using just 3.7M parameters. We report the results of our network on the test benchmark of ScanNet in Table 3, which validates that PicassoNet-II is very competitive to the top performer. We note that PicassoNet-II takes 58 ms on average to process per (voxelized) mesh on a single NVIDIA RTX 3090 GPU.

## 8 FURTHER ANALYSIS

In this section, we provide further results to analyze the proposed approach.

### 8.1 Varying the Number of vMF Components

We study influence of the number of components in the vMF mixture, *e.g.*  $T = 27, 18, 9$ , on the performance of PicassoNet-II. We use S3DIS as well as ScanNet for this analysis. We use the validation set of ScanNet for all experiments for analysis. Table 4 summarizes the segmentation results. It can be noticed that generally, larger number of  $T$  leads to more accurate predictions because it introduces more filter parameters. By default, PicassoNet-II selects  $T$  as 27.

### 8.2 Performance with Different Input Features

We also analyze the performance of PicassoNet-II for different facet features, including geometrics and textures. Firstly, we fix the facet textures as ‘plain’ vertex colors, *i.e.*  $(\alpha, \beta) = (0, 1)$ , and compare the network performance for two different facet geometrics. One is composed of

TABLE 4  
Performance of PicassoNet-II by using different number of components in the vMF mixture.

| Dataset | S3DIS Area 5 |      |      | ScanNet |      |      |
|---------|--------------|------|------|---------|------|------|
|         | Number $T$   | 27   | 18   | 9       | 27   | 18   |
| mIoU    |              | 69.4 | 68.8 | 68.4    | 71.9 | 71.8 |

TABLE 5  
Performance of PicassoNet-II by taking different geometric and texture features for the mesh facets.

| Dataset    | ScanNet                                      |   | S3DIS   |   |      |
|------------|--|---|---|---|------|
|            | Textures $(\alpha, \beta)$                   | $(0, 1)$  | $(0, 1)$  | $(3, 3)$  |      |
| Geometrics | $[\mathbf{x}_1, \mathbf{x}_2, \mathbf{x}_3]$ | $[\ell, \boldsymbol{\theta}, \mathbf{n}, \mathbf{h}]$ | $[\ell, \boldsymbol{\theta}, \mathbf{n}, \mathbf{h}]$ | $[\ell, \boldsymbol{\theta}, \mathbf{n}, \mathbf{h}]$ |      |
| mIoU       |  | 71.0  | 71.9  | 69.4  | 69.8 |

vertex coordinates, *i.e.*  $[\mathbf{x}_1, \mathbf{x}_2, \mathbf{x}_3]$ , the other is the proposed  $[\ell, \boldsymbol{\theta}, \mathbf{n}, \mathbf{h}]$  in § 4.4. ScanNet is used in this experiment. Our results in Table 5 suggest that the proposed facet geometrics is a better alternative for the vertex coordinates. Further, to compare the network performance for ‘plain’ and ‘rendered’ facet textures, we render the mesh facets of S3DIS dataset by setting  $(\alpha, \beta) = (3, 3)$  in Eq. (6) and fix the geometric features as  $[\ell, \boldsymbol{\theta}, \mathbf{n}, \mathbf{h}]$ . These results are also summarized in Table 5. It can be noticed that finer textures indeed boost the network performance, as expected.

### 8.3 Is Dual Convolution Always Necessary?

It is known that point cloud convolutions can be time-consuming because of neighborhood search, which accompanies a significant computational burden in processing dense data [18]. The DCM-Net and original PicassoNet [38] use dual convolutions in every layer of their networks. In

TABLE 6

Performance and runtime of the network while adding or deleting point cloud convolutions to PicassoNet-II. The list of NN search radii 0.1, 0.2, 0.4, 0.8 in the parenthesis denotes radius of neighborhood search for point cloud convolutions from resolution  $\mathcal{T}^2$  to  $\mathcal{T}^5$ . The dual levels of  $(\mathcal{T}^3, \mathcal{T}^4, \mathcal{T}^5)$  in the third column correspond to the actual configurations of PicassoNet-II.

| Config              | adding   | used  | reducing                         |
|---------------------|--|---|----------------------------------|
| Dual Levels         | $(\mathcal{T}^2, \mathcal{T}^3, \mathcal{T}^4, \mathcal{T}^5)$ | $(\mathcal{T}^3, \mathcal{T}^4, \mathcal{T}^5)$ | $(\mathcal{T}^4, \mathcal{T}^5)$ |
| NN search radii     | (0.1, 0.2, 0.4, 0.8)   | (0.2, 0.4, 0.8)                                 | (0.4, 0.8)                       |
| Inference time (ms) | 93   | 58  | 52                               |
| mIoU                | 71.7   | 71.9  | 71.0                             |

TABLE 7

Network performance on the HUMAN dataset while adding or deleting point cloud convolutions from PicassoNet-II.

| Dual  | $(\mathcal{T}^2, \mathcal{T}^3, \mathcal{T}^4, \mathcal{T}^5)$ | $(\mathcal{T}^3, \mathcal{T}^4, \mathcal{T}^5)$ | $(\mathcal{T}^4, \mathcal{T}^5)$ | $(\mathcal{T}^5)$ | None |
|-------|--|---|----------------------------------|-------------------|------|
| Radii | (0.1, 0.2, 0.4, 0.8)   | (0.2, 0.4, 0.8)                                 | (0.4, 0.8)                       | (0.8)             | N.A. |
| Acc   | 91.3   | 91.4  | 91.0                             | 90.7              | 89.2 |

comparison, PicassoNet-II utilizes dual convolutions only in its encoder blocks of coarse resolutions  $\mathcal{T}^{3\sim 5}$ . To consolidate our pruning of point-based convolutions for PicassoNet-II, we empirically evaluate if dual convolution is necessary for every layer. In specific, we alter the PicassoNet-II by either adding point cloud convolutions to its encoders of resolution  $\mathcal{T}^2$ , or removing its existing point cloud convolution from the encoder of resolution  $\mathcal{T}^3$ . We test the performance of these variants, and report their results as well as other details in Table 6. ScanNet dataset is utilized in this experiment. From our findings, we can conclude that point-based convolutions can be eliminated from high resolution layers of the network, without affecting the network performance. This led us to our eventual configuration of PicassoNet-II, which is both effective and efficient. The reported inference time in the Table is for voxelized meshes of grid size  $2cm$ . To further confirm our finding, we also conducted a similar experiment on the HUMAN dataset. The results in Table 7 validate our insight about the passive role of dual convolutions for dense meshes.

### 8.4 2D Embedding of the Shape Features

We visualize the shape features learned by PicassoNet-II for the test samples of ShapeNetCore [39] by showing their 2D embeddings in Fig. 6 using the t-SNE technique [99] for dimension reduction. For the feature representations, we use the 256-dimensional output of global pooling in the classification network. From Fig. 6, it is clear that the shapes of most classes are distinctly represented, such as *car*, *bus*, *guitar*, *knife*, *vessel*, *rifle*, *faucet*, *airplane*, *chair*, *sofa*, *table*, etc. We also note that some classes are much closer to each other such that their closeness is well-justified based on their shapes and semantics. For instance, buses are close to cars and pistols are close to rifles.

### 8.5 Semantic Parsing Visualization

As representative examples, we visualize the semantic parsing results of PicassoNet-II for shapes of human bodies [42] and surfaces of real-world scenes [3] in Fig. 7. The network predicts most of the body parts and scene objects correctly. However, we see that segmenting parts and objects near boundaries sometimes cause minor issues for our network.

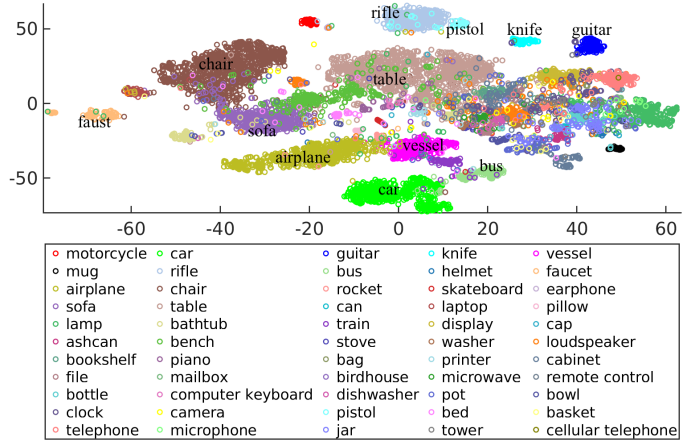


Fig. 6. 2D embedding of the shape feature representations learned by PicassoNet-II for the test samples of ShapeNetCore.

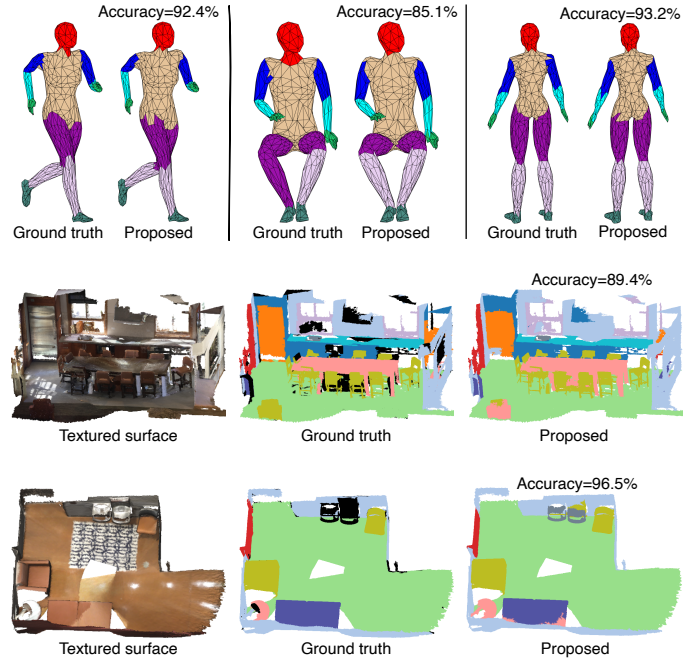


Fig. 7. The ground truth and our predictions for the shapes of human bodies and real-world scene surfaces. The black colors in the ground truth of textured surfaces indicate unlabelled objects.

Nevertheless, such errors remain minor and do not occur too frequently. Also notice that one of the test samples of human bodies has incorrect ground-truth label for the right leg. Such ground truth problems can result in a lower accuracy value of an accurate technique like ours. This also indicates that instead of highest prediction performance on a single dataset, highly competitive results across multiple datasets is sometimes more preferable in this domain. Our PicassoNet-II is able to achieve that.

## 9 CONCLUSION

We made two major contributions towards hierarchical neural modeling of heterogeneous 3D meshes. First, we presented Picasso - a modular implementation of multiple desired operations for geometric feature learning over 3D meshes. Picasso introduces novel mesh-amenable convolutional operations, mesh (un)poolings and GPU-accelerated

mesh decimation. This article considerably enhances our preliminary version of Picasso by incorporating fuzzy modeling modules and improved efficiency. Moreover, we also release Pytorch version of Picasso with this article along with the Tensorflow support. The second major contribution of this article is our network, PicassoNet-II. Enabled by the upgraded Picasso, our network is able to effectively process facet signals, including primitive geometrics and textures, as inputs. It also takes advantage of a new insight provided in this article regarding the passive role of dual convolutions in high resolution mesh feature learning. Leveraging that, PicassoNet-II learns geometric features over 3D shapes and scene surfaces efficiently. Through extensive experiments, we established highly competitive performance of PicassoNet-II for shape analysis and scene parsing.

## ACKNOWLEDGMENTS

Professor Ajmal Mian is the recipient of an Australian Research Council Future Fellowship (project number FT210100268) funded by the Australian Government. Dr. Naveed Akhtar is the recipient of Office of National Intelligence Postdoctoral Grant (project number NIPG-2021-001) funded by the Australian Government.

## REFERENCES

- [1] R. Hanocka, A. Hertz, N. Fish, R. Giryes, S. Fleishman, and D. Cohen-Or, "MeshCNN: a network with an edge," *ACM Transactions on Graphics (TOG)*, vol. 38, no. 4, pp. 1–12, 2019.
- [2] A. Ranjan, T. Bolkart, S. Sanyal, and M. J. Black, "Generating 3d faces using convolutional mesh autoencoders," in *Proceedings of the European Conference on Computer Vision (ECCV)*, 2018, pp. 704–720.
- [3] A. Dai, A. X. Chang, M. Savva, M. Halber, T. Funkhouser, and M. Nießner, "ScanNet: Richly-annotated 3d reconstructions of indoor scenes," in *Proceedings of the IEEE Conference on Computer Vision and Pattern Recognition*, 2017, pp. 5828–5839.
- [4] B.-S. Hua, Q.-H. Pham, D. T. Nguyen, M.-K. Tran, L.-F. Yu, and S.-K. Yeung, "Scenenn: A scene meshes dataset with annotations," in *International Conference on 3D Vision (3DV)*, 2016.
- [5] A. Chang, A. Dai, T. Funkhouser, M. Halber, M. Niessner, M. Savva, S. Song, A. Zeng, and Y. Zhang, "Matterport3d: Learning from rgb-d data in indoor environments," *International Conference on 3D Vision (3DV)*, 2017.
- [6] K. He, X. Zhang, S. Ren, and J. Sun, "Deep residual learning for image recognition," in *Proceedings of the IEEE conference on computer vision and pattern recognition*, 2016, pp. 770–778.
- [7] A. Krizhevsky, I. Sutskever, and G. E. Hinton, "ImageNet classification with deep convolutional neural networks," in *Advances in Neural Information Processing Systems*, 2012, pp. 1097–1105.
- [8] W. Liu, D. Anguelov, D. Erhan, C. Szegedy, S. Reed, C.-Y. Fu, and A. C. Berg, "SSD: Single shot multibox detector," in *European Conference on Computer Vision*, 2016, pp. 21–37.
- [9] J. Long, E. Shelhamer, and T. Darrell, "Fully convolutional networks for semantic segmentation," in *Proceedings of the IEEE Conference on Computer Vision and Pattern Recognition*, 2015, pp. 3431–3440.
- [10] J. Redmon, S. Divvala, R. Girshick, and A. Farhadi, "You only look once: Unified, real-time object detection," in *Proceedings of the IEEE conference on Computer Vision and Pattern Recognition*, 2016, pp. 779–788.
- [11] S. Ren, K. He, R. Girshick, and J. Sun, "Faster r-cnn: Towards real-time object detection with region proposal networks," in *Advances in Neural Information Processing Systems*, 2015, pp. 91–99.
- [12] O. Ronneberger, P. Fischer, and T. Brox, "U-net: Convolutional networks for biomedical image segmentation," in *International Conference on Medical Image Computing and Computer-Assisted Intervention*, 2015, pp. 234–241.
- [13] K. Simonyan and A. Zisserman, "Very deep convolutional networks for large-scale image recognition," *International Conference on Learning Representations*, 2015.
- [14] N. Verma, E. Boyer, and J. Verbeek, "Featnet: Feature-steered graph convolutions for 3d shape analysis," in *Proceedings of the IEEE conference on computer vision and pattern recognition*, 2018, pp. 2598–2606.
- [15] J. Schult, F. Engelmann, T. Kontogianni, and B. Leibe, "Dualconvmesh-net: Joint geodesic and euclidean convolutions on 3d meshes," in *Proceedings of the IEEE/CVF Conference on Computer Vision and Pattern Recognition*, 2020, pp. 8612–8622.
- [16] M. M. Bronstein, J. Bruna, Y. LeCun, A. Szlam, and P. Vandergheynst, "Geometric deep learning: going beyond euclidean data," *IEEE Signal Processing Magazine*, vol. 34, no. 4, pp. 18–42, 2017.
- [17] L. Yi, V. G. Kim, D. Ceylan, I. Shen, M. Yan, H. Su, A. Lu, Q. Huang, A. Sheffer, L. Guibas *et al.*, "A scalable active framework for region annotation in 3D shape collections," *ACM Transactions on Graphics*, vol. 35, no. 6, p. 210, 2016.
- [18] H. Lei, N. Akhtar, and A. Mian, "Spherical kernel for efficient graph convolution on 3d point clouds," *IEEE Transactions on Pattern Analysis and Machine Intelligence*, 2020.
- [19] S. Song, S. P. Lichtenberg, and J. Xiao, "SUN RGB-D: A RGB-D scene understanding benchmark suite," in *Proceedings of the IEEE Conference on Computer Vision and Pattern Recognition*, 2015, pp. 567–576.
- [20] I. Armeni, O. Sener, A. R. Zamir, H. Jiang, I. Brilakis, M. Fischer, and S. Savarese, "3D semantic parsing of large-scale indoor spaces," in *Proceedings of the IEEE Conference on Computer Vision and Pattern Recognition*, 2016, pp. 1534–1543.
- [21] D. Boscaini, J. Masci, E. Rodolà, and M. Bronstein, "Learning shape correspondence with anisotropic convolutional neural networks," in *Advances in neural information processing systems*, 2016, pp. 3189–3197.
- [22] F. Monti, D. Boscaini, J. Masci, E. Rodola, J. Svoboda, and M. M. Bronstein, "Geometric deep learning on graphs and manifolds using mixture model cnns," in *Proceedings of the IEEE Conference on Computer Vision and Pattern Recognition*, 2017, pp. 5115–5124.
- [23] J. Xie, Y. Fang, F. Zhu, and E. Wong, "Deepshape: Deep learned shape descriptor for 3d shape matching and retrieval," in *Proceedings of the IEEE Conference on Computer Vision and Pattern Recognition*, 2015, pp. 1275–1283.
- [24] M. Garland, "Quadric-based polygonal surface simplification [thesis]," *Pittsburgh: Carnegie Mellon University*, 1999.
- [25] M. Garland and P. S. Heckbert, "Surface simplification using quadric error metrics," in *Proceedings of the 24th annual conference on Computer graphics and interactive techniques*, 1997, pp. 209–216.
- [26] J. Rossignac and P. Borrel, "Multi-resolution 3d approximations for rendering complex scenes," in *Modeling in computer graphics*. Springer, 1993, pp. 455–465.
- [27] Q.-Y. Zhou, J. Park, and V. Koltun, "Open3D: A modern library for 3D data processing," *arXiv preprint arXiv:1801.09847*, 2018.
- [28] C. Choy, J. Gwak, and S. Savarese, "4d spatio-temporal convnets: Minkowski convolutional neural networks," *Proceedings of the IEEE conference on computer vision and pattern recognition*, 2019.
- [29] H. Thomas, C. R. Qi, J.-E. Deschaud, B. Marcotegui, F. Goulette, and L. J. Guibas, "Kpconv: Flexible and deformable convolution for point clouds," *Proceedings of the IEEE International Conference on Computer Vision*, 2019.
- [30] B. Graham and L. van der Maaten, "Submanifold sparse convolutional networks," *arXiv preprint arXiv:1706.01307*, 2017.
- [31] W. Wu, Z. Qi, and L. Fuxin, "Pointconv: Deep convolutional networks on 3d point clouds," in *Proceedings of the IEEE Conference on Computer Vision and Pattern Recognition*, 2019, pp. 9621–9630.
- [32] C. R. Qi, L. Yi, H. Su, and L. J. Guibas, "PointNet++: Deep hierarchical feature learning on point sets in a metric space," *Advances in Neural Information Processing Systems*, 2017.
- [33] H. Su, V. Jampani, D. Sun, S. Maji, E. Kalogerakis, M.-H. Yang, and J. Kautz, "SPLATNet: Sparse lattice networks for point cloud processing," in *Proceedings of the IEEE Conference on Computer Vision and Pattern Recognition*, 2018, pp. 2530–2539.
- [34] M. Abadi, P. Barham, J. Chen, Z. Chen, A. Davis, J. Dean, M. Devin, S. Ghemawat, G. Irving, M. Isard *et al.*, "Tensorflow: A system for large-scale machine learning," in *12th {USENIX} Symposium on Operating Systems Design and Implementation ({OSDI} 16)*, 2016, pp. 265–283.
- [35] A. Paszke, S. Gross, F. Massa, A. Lerer, J. Bradbury, G. Chanan, T. Killeen, Z. Lin, N. Gimelshein, L. Antiga *et al.*, "Pytorch: An imperative style, high-performance deep learning library," *Advances in neural information processing systems*, vol. 32, pp. 8026–8037, 2019.



- [36] J. Huang, H. Zhang, L. Yi, T. Funkhouser, M. Nießner, and L. J. Guibas, "TextureNet: Consistent local parametrizations for learning from high-resolution signals on meshes," in *Proceedings of the IEEE Conference on Computer Vision and Pattern Recognition*, 2019, pp. 4440–4449.
- [37] S. Gopal and Y. Yang, "Von mises-fisher clustering models," in *International Conference on Machine Learning*. PMLR, 2014, pp. 154–162.
- [38] H. Lei, N. Akhtar, and A. Mian, "Picasso: A cuda-based library for deep learning over 3d meshes," in *Proceedings of the IEEE Conference on Computer Vision and Pattern Recognition*, 2021.
- [39] A. X. Chang, T. Funkhouser, L. Guibas, P. Hanrahan, Q. Huang, Z. Li, S. Savarese, M. Savva, S. Song, H. Su *et al.*, "ShapeNet: An information-rich 3D model repository," *arXiv preprint arXiv:1512.03012*, 2015.
- [40] Z. Lian, A. Godil, B. Bustos, M. Daoudi, J. Hermans, S. Kawamura, Y. Kurita, G. Lavoua, and P. Dp Suetens, "Shape retrieval on non-rigid 3d watertight meshes," in *Eurographics workshop on 3d object retrieval*, 2011.
- [41] Y. Wang, S. Asafi, O. Van Kaick, H. Zhang, D. Cohen-Or, and B. Chen, "Active co-analysis of a set of shapes," *ACM Transactions on Graphics (TOG)*, vol. 31, no. 6, pp. 1–10, 2012.
- [42] H. Maron, M. Galun, N. Aigerman, M. Trope, N. Dym, E. Yumer, V. G. Kim, and Y. Lipman, "Convolutional neural networks on surfaces via seamless toric covers." *ACM Trans. Graph.*, vol. 36, no. 4, pp. 71–1, 2017.
- [43] F. Bogo, J. Romero, M. Loper, and M. J. Black, "Faust: Dataset and evaluation for 3d mesh registration," in *Proceedings of the IEEE Conference on Computer Vision and Pattern Recognition*, 2014, pp. 3794–3801.
- [44] H. Lei, N. Akhtar, and A. Mian, "Seggcn: Efficient 3d point cloud segmentation with fuzzy spherical kernel," in *Proceedings of the IEEE/CVF Conference on Computer Vision and Pattern Recognition*, 2020, pp. 11 611–11 620.
- [45] Z. Wu, S. Song, A. Khosla, F. Yu, L. Zhang, X. Tang, and J. Xiao, "3D ShapeNets: A deep representation for volumetric shapes," in *Proceedings of the IEEE Conference on Computer Vision and Pattern Recognition*, 2015, pp. 1912–1920.
- [46] D. Maturana and S. Scherer, "VoxNet: A 3D convolutional neural network for real-time object recognition," in *IEEE/RSJ International Conference on Intelligent Robots and Systems*. IEEE, 2015, pp. 922–928.
- [47] J. Huang and S. You, "Point cloud labeling using 3D convolutional neural network," in *International Conference on Pattern Recognition*, 2016, pp. 2670–2675.
- [48] N. Sedaghat, M. Zolfaghari, and T. Brox, "Orientation-boosted voxel nets for 3D object recognition," *arXiv preprint arXiv:1604.03351*, 2016.
- [49] A. Zeng, S. Song, M. Nießner, M. Fisher, J. Xiao, and T. Funkhouser, "3DMatch: Learning local geometric descriptors from RGB-D reconstructions," in *Proceedings of the IEEE Conference on Computer Vision and Pattern Recognition*, 2017, pp. 199–208.
- [50] Y. Zhang, M. Bai, P. Kohli, S. Izadi, and J. Xiao, "Deepcontext: Context-encoding neural pathways for 3D holistic scene understanding," in *Proceedings of the IEEE International Conference on Computer Vision*, 2017, pp. 1192–1201.
- [51] M. Engelcke, D. Rao, D. Zeng Wang, C. Hay Tong, and I. Posner, "Vote3Deep: Fast object detection in 3D point clouds using efficient convolutional neural networks," in *IEEE International Conference on Robotics and Automation*, June 2017.
- [52] B. Graham, M. Engelcke, and L. van der Maaten, "3D semantic segmentation with submanifold sparse convolutional networks," *Proceedings of the IEEE Computer Vision and Pattern Recognition*, pp. 18–22, 2018.
- [53] Y. Li, S. Pirk, H. Su, C. R. Qi, and L. J. Guibas, "FPNN: Field probing neural networks for 3D data," in *Advances in Neural Information Processing Systems*, 2016, pp. 307–315.
- [54] B.-S. Hua, M.-K. Tran, and S.-K. Yeung, "Pointwise convolutional neural networks," in *Proceedings of the IEEE Conference on Computer Vision and Pattern Recognition*, 2018, pp. 984–993.
- [55] G. Riegler, A. Osman Ulusoy, and A. Geiger, "OctNet: Learning deep 3d representations at high resolutions," in *Proceedings of the IEEE Conference on Computer Vision and Pattern Recognition*, 2017, pp. 3577–3586.
- [56] H. Tang, Z. Liu, S. Zhao, Y. Lin, J. Lin, H. Wang, and S. Han, "Searching efficient 3d architectures with sparse point-voxel convolution," in *European Conference on Computer Vision*. Springer, 2020, pp. 685–702.
- [57] M. Tatarchenko, J. Park, V. Koltun, and Q.-Y. Zhou, "Tangent convolutions for dense prediction in 3d," in *Proceedings of the IEEE Conference on Computer Vision and Pattern Recognition*, 2018, pp. 3887–3896.
- [58] M. Atzmon, H. Maron, and Y. Lipman, "Point convolutional neural networks by extension operators," *ACM Transactions on Graphics (TOG)*, vol. 37, no. 3, 2018.
- [59] C. R. Qi, H. Su, K. Mo, and L. J. Guibas, "PointNet: Deep learning on point sets for 3D classification and segmentation," *Proceedings of the IEEE Conference on Computer Vision and Pattern Recognition*, pp. 652–660, 2017.
- [60] R. Klokov and V. Lempitsky, "Escape from cells: Deep kd-networks for the recognition of 3d point cloud models," in *Proceedings of the IEEE International Conference on Computer Vision*. IEEE, 2017, pp. 863–872.
- [61] J. Li, B. M. Chen, and G. H. Lee, "So-net: Self-organizing network for point cloud analysis," in *Proceedings of the IEEE Conference on Computer Vision and Pattern Recognition*, 2018, pp. 9397–9406.
- [62] D. Rethage, J. Wald, J. Sturm, N. Navab, and F. Tombari, "Fully-convolutional point networks for large-scale point clouds," in *Proceedings of the European Conference on Computer Vision (ECCV)*, 2018, pp. 596–611.
- [63] Y. Shen, C. Feng, Y. Yang, and D. Tian, "Mining point cloud local structures by kernel correlation and graph pooling," in *Proceedings of the IEEE Conference on Computer Vision and Pattern Recognition*, vol. 4, 2018.
- [64] L. Yi, H. Su, X. Guo, and L. J. Guibas, "Syncspecnn: Synchronized spectral cnn for 3d shape segmentation," in *Proceedings of the IEEE Conference on Computer Vision and Pattern Recognition*, 2017, pp. 2282–2290.
- [65] M. Simonovsky and N. Komodakis, "Dynamic edge-conditioned filters in convolutional neural networks on graphs," in *Proceedings of the IEEE Conference on Computer Vision and Pattern Recognition*, 2017.
- [66] B. De Brabandere, X. Jia, T. Tuytelaars, and L. Van Gool, "Dynamic filter networks," in *Advances in Neural Information Processing Systems*, 2016.
- [67] F. Groh, P. Wieschollek, and H. P. Lensch, "Flex-convolution," in *Asian Conference on Computer Vision*. Springer, 2018, pp. 105–122.
- [68] Y. Li, R. Bu, M. Sun, W. Wu, X. Di, and B. Chen, "PointCNN: Convolution on x-transformed points," in *Advances in Neural Information Processing Systems*, 2018, pp. 820–830.
- [69] L. Wang, Y. Huang, Y. Hou, S. Zhang, and J. Shan, "Graph attention convolution for point cloud semantic segmentation," in *The IEEE Conference on Computer Vision and Pattern Recognition*, June 2019.
- [70] Y. Xu, T. Fan, M. Xu, L. Zeng, and Y. Qiao, "Spidernn: Deep learning on point sets with parameterized convolutional filters," in *Proceedings of the European Conference on Computer Vision*, 2018, pp. 87–102.
- [71] H. Lei, N. Akhtar, and A. Mian, "Octree guided cnn with spherical kernels for 3d point clouds," in *Proceedings of the IEEE Conference on Computer Vision and Pattern Recognition*, 2019, pp. 9631–9640.
- [72] M. Xu, R. Ding, H. Zhao, and X. Qi, "Paconv: Position adaptive convolution with dynamic kernel assembling on point clouds," in *Proceedings of the IEEE/CVF Conference on Computer Vision and Pattern Recognition*, 2021, pp. 3173–3182.
- [73] A. Vaswani, N. Shazeer, N. Parmar, J. Uszkoreit, L. Jones, A. N. Gomez, Ł. Kaiser, and I. Polosukhin, "Attention is all you need," in *Advances in neural information processing systems*, 2017, pp. 5998–6008.
- [74] H. Zhao, L. Jiang, J. Jia, P. Torr, and V. Koltun, "Point transformer," 2021.
- [75] J. Masci, D. Boscaini, M. Bronstein, and P. Vandergheynst, "Geodesic convolutional neural networks on riemannian manifolds," in *Proceedings of the IEEE international conference on computer vision workshops*, 2015, pp. 37–45.
- [76] M. Defferrard, X. Bresson, and P. Vandergheynst, "Convolutional neural networks on graphs with fast localized spectral filtering," in *Advances in Neural Information Processing Systems*, 2016, pp. 3844–3852.
- [77] F. Milano, A. Loquercio, A. Rosinol, D. Scaramuzza, and L. Carlone, "Primal-dual mesh convolutional neural networks," in *Advances in Neural Information Processing Systems*, 2020.

- [78] M. Fey and J. E. Lenssen, "Fast graph representation learning with pytorch geometric," *arXiv preprint arXiv:1903.02428*, 2019.
- [79] Y. Wang, Y. Sun, Z. Liu, S. E. Sarma, M. M. Bronstein, and J. M. Solomon, "Dynamic graph cnn for learning on point clouds," *arXiv preprint arXiv:1801.07829*, 2018.
- [80] Z. Hu, X. Bai, J. Shang, R. Zhang, J. Dong, X. Wang, G. Sun, H. Fu, and C.-L. Tai, "Vmnet: Voxel-mesh network for geodesic-aware 3d semantic segmentation," 2021.
- [81] T. Chen, S. Kornblith, M. Norouzi, and G. Hinton, "A simple framework for contrastive learning of visual representations," in *International conference on machine learning*. PMLR, 2020, pp. 1597–1607.
- [82] F. Chollet, "Xception: Deep learning with depthwise separable convolutions," in *Proceedings of the IEEE conference on computer vision and pattern recognition*, 2017, pp. 1251–1258.
- [83] V. Nair and G. E. Hinton, "Rectified linear units improve restricted boltzmann machines," in *ICML*, 2010, pp. 807–814.
- [84] H. S. M. Coxeter, "Introduction to geometry," 1961.
- [85] G. Huang, Z. Liu, L. Van Der Maaten, and K. Q. Weinberger, "Densely connected convolutional networks," in *Proceedings of the IEEE conference on computer vision and pattern recognition*, 2017, pp. 4700–4708.
- [86] C. Szegedy, W. Liu, Y. Jia, P. Sermanet, S. Reed, D. Anguelov, D. Erhan, V. Vanhoucke, and A. Rabinovich, "Going deeper with convolutions," in *Proceedings of the IEEE Conference on Computer Vision and Pattern Recognition*, 2015.
- [87] F. P. Preparata and M. I. Shamos, *Computational geometry: an introduction*. Springer Science & Business Media, 2012.
- [88] N. Srivastava, G. Hinton, A. Krizhevsky, I. Sutskever, and R. Salakhutdinov, "Dropout: a simple way to prevent neural networks from overfitting," *The journal of machine learning research*, vol. 15, no. 1, pp. 1929–1958, 2014.
- [89] D. P. Kingma and J. Ba, "Adam: A method for stochastic optimization," *International Conference on Learning Representations*, 2015.
- [90] A. Sinha, J. Bai, and K. Ramani, "Deep learning 3d shape surfaces using geometry images," in *European conference on computer vision*. Springer, 2016, pp. 223–240.
- [91] D. Ezuz, J. Solomon, V. G. Kim, and M. Ben-Chen, "Gwcnn: A metric alignment layer for deep shape analysis," in *Computer Graphics Forum*, vol. 36, no. 5. Wiley Online Library, 2017, pp. 49–57.
- [92] S. Xie, J. Gu, D. Guo, C. R. Qi, L. Guibas, and O. Litany, "Pointcontrast: Unsupervised pre-training for 3d point cloud understanding," in *European Conference on Computer Vision*. Springer, 2020, pp. 574–591.
- [93] "Surface Reconstruction from Scattered Points, Mathworks 2020," <https://au.mathworks.com>, accessed 17-Nov-2020.
- [94] L. J. Latecki and R. Lakamper, "Shape similarity measure based on correspondence of visual parts," *IEEE Transactions on Pattern Analysis and Machine Intelligence*, vol. 22, no. 10, pp. 1185–1190, 2000.
- [95] L. Tchapmi, C. Choy, I. Armeni, J. Gwak, and S. Savarese, "Seg-cloud: Semantic segmentation of 3d point clouds," in *International Conference on 3D Vision*. IEEE, 2017, pp. 537–547.
- [96] L. Landrieu and M. Simonovsky, "Large-scale point cloud semantic segmentation with superpoint graphs," in *Proceedings of the IEEE Conference on Computer Vision and Pattern Recognition*, 2018.
- [97] L. Landrieu and M. Boussaha, "Point cloud oversegmentation with graph-structured deep metric learning," *Proceedings of the IEEE conference on computer vision and pattern recognition*, 2019.
- [98] L. Wang, Y. Huang, Y. Hou, S. Zhang, and J. Shan, "Graph attention convolution for point cloud semantic segmentation," in *Proceedings of the IEEE Conference on Computer Vision and Pattern Recognition*, 2019, pp. 10 296–10 305.
- [99] L. Van der Maaten and G. Hinton, "Visualizing data using t-sne." *Journal of machine learning research*, vol. 9, no. 11, 2008.